Dynamic Landslide Processes Revealed by Broadband Seismic Records

Masumi Yamada,[1] Hiroyuki Kumagai,[2,3] Yuki Matsushi,[1] Takanori Matsuzawa[2]

We use broadband seismic recordings to trace the dynamic process of the deep-seated Akatani landslide that occurred on the Kii Peninsula, Japan, which is one of the best recorded large slope failures. Combining analyses of the seismic records with precise topographic surveys done before and after the event, we can resolve a detailed time history of the mass movement. During 50 s of the large landslide, we observe a smooth initiation, acceleration with changes in basal friction, and reversal of the momentum when the mass collides with the opposite valley wall. Of particular importance is the determination of the dynamic friction during the landslide. The coefficient of friction is estimated to be 0.56 at the beginning of the event and drops to 0.38 for most of the sliding. The change in the frictional level on the sliding surface may be due to liquefaction or breaking of rough patches, and contributes to the extended propagation of the large landslide.

1. Introduction

Assessing and managing the risks posed by deep-seated catastrophic landslides requires a quantitative understanding of the dynamics of sliding rock masses. Previously, landslide motion has been inferred qualitatively from topographic changes caused by the event, and occasionally from eyewitness reports. However, these conventional approaches are unable to evaluate source processes and dynamic parameters. In this study, we used ground shaking data recorded away from the landslide for reconstructing the dynamic landslide processes. The deep-seated catastrophic landslide sequence induced by heavy rainfall in 2011 in the Kii Peninsula, Japan, was the first instance in which 1) seismic signals radiated by landslides were recorded by densely distributed near-source seismometers [*Yamada et al.*, 2012], and 2) the precise volume of the landslide material was able to be measured by comparing pre- and post-landslide topographic data obtained using airborne laser scanning. We performed a source inversion with the long-period seismic records [*Kanamori and Given*, 1982; *Brodsky et al.*, 2003; *Lin et al.*, 2010; *Moretti et al.*, 2012] of one of the largest events, and from this obtained a force history of the landslide. Here we reveal the dynamic processes of the landslide: smooth initiation of sliding, acceleration accompanied by a substantial decrease in frictional force, and deceleration due to collision. The approach demonstrated here offers an innovative method for understanding the sliding processes associated with catastrophic landslides, enabling us to simulate the motion of such events.

[1]Disaster Prevention Research Institute, Kyoto University, Gokasho, Uji, Kyoto 611-0011, Japan
[2]National Research Institute for Earth Science and Disaster Prevention, 3-1 Tennodai, Tsukuba, Ibaraki 305-0006, Japan
[3]Now at Graduate School of Environmental Studies, Nagoya University, Chikusa, Nagoya, Aichi 464-8601, Japan

0094-8276/13/$5.00

2. Data and Methods

On 3–4 September 2011, extensive slope failures occurred across a wide region of the Kii Peninsula as Typhoon Talas produced heavy rainfalls across western Japan. The Akatani landslide, one of the largest events, occurred at 16:21:30 on 4 September 2011 (JST) in Nara prefecture, central Japan (135.725°N, 34.126°E) [*Yamada et al.*, 2012]. There was extensive mass movement on a slope approximately 1 km long, inclined at an angle of 30° (Figures 1a and 1b). We were able to calculate the volume of the landslide from precise measurement of topographic data using airborne laser scanning (LiDAR) which was done both before and after the event. The volume was 8.2×10^6 m^3 [*Yamada et al.*, 2012] and the total mass (m) of displaced material is estimated to be 2.1×10^{10} kg, assuming an average soil density of 2600 kg/m^3 [*Iwaya and Kano*, 2005]. The vertical displacement of the center of the mass is calculated as 265 m, and the potential energy released from this event is estimated to be $5.5 \times 10^{13} J$.

We performed a waveform inversion using six broadband seismic stations to obtain the source time function using the station distribution shown in Figure S1. The source-station distances of these stations range from 35 to 200 km. We processed the broadband records according to the following procedure. First, we removed the mean from the time series and corrected for the instrumental response in all waveforms. The records were then integrated once in the time domain, and a non-causal fourth order Butterworth filter (0.01 and 0.1 Hz) was applied. We determined these corner frequencies to maximize the frequency band and minimize the effect of structural heterogeneities. We then decimated the data by a factor of 20, reducing the sampling frequency to 1 Hz. We used these filtered displacement records for the inversion.

Following the method of *Nakano et al.* [2008], we performed a waveform inversion in the frequency domain to determine the source process of the landslide. We calculated Green's functions at source nodes on the grid shown in Figure S1, using the discrete wavenumber method [*Bouchon*, 1979] and the Japan Meteorological Agency (JMA) one-dimensional structure model [*Ueno et al.*, 2002]. Assuming a single-force mechanism for the landslide source [*Hasegawa and Kanamori*, 1987], we estimated the least-squares solution in the frequency domain. We performed an inverse Fourier transform on the solution to determine source time functions for three single-force components at each source node [*Nakano et al.*, 2008]. We performed a grid search in space and the normalized residual contour is shown in Figure S1. The best-fit source location was determined at a position very close to the actual Akatani landslide, and the estimated source time functions shown in Figure S2a were stable in the region of the best-fit location.

3. Estimated Source Time Functions

The resultant source time functions for the three single force components along with the waveform fits between observed and synthetic seismograms are shown in Figure S2. The particle motion of the horizontal source time functions in Figure 1c indicates that the forces act in one dominant direction (130° from North), consistent with the direction of mass sliding. Therefore, we rotated the two horizontal components to the 130° and 220° directions (Figure 2a). Note that the positive direction of the N130°E component is upslope.

The source time functions estimated from the long-period waveform inversion reveal the dynamic history of the landslide. The notably small amplitude of the N220°E (N140°W) component indicates that mass movement in this direction is negligible. The waveforms of the N130°E (radial) and vertical components are highly coherent. We interpret these waveforms as being representative of three stages in the landslide process (see Figures 2a and 2b).

During the first stage (90–112 s), the mass starts moving and accelerates down the slope. The force acting on the ground is in the opposite direction to the inertial force acting on the mass. The particle motion derived from the vertical and radial components in Figure 1d shows that the direction of the force is parallel to the updip direction of the slope. In the second stage (112–132 s), the toe of the mass reaches the end of the slope and the mass starts decelerating. The sliding mass pushes toward the opposite side of the valley, and the direction of the force acting on the ground is reversed from that in the first stage. Due to this change in direction, the phase of the horizontal and vertical components is shifted (see Figures 1b and 1d). When the leading edge of the mass reaches the end of the slope, a downward-directed vertical force acts on the ground. The mass continues to move toward the other side of the valley, producing a contact force in the horizontal direction. The amplitudes of the waveforms during the third stage (132–140 s) is relatively small, and the force in the vertical cross-section is directed approximately parallel to the sliding slope. This may indicate that the mass slightly ran up on the sliding slope and the movement terminated with some plastic deformation.

4. Dynamic History of the Landslide

As the estimated source time functions are equivalent to the inertial force of the sliding mass [*Kanamori and Given*, 1982], the velocity and displacement of the mass can be calculated from the source time functions. The velocity (v) is the integral of the single force (f) divided by the mass (i.e. $v = \int f dt/m$), and the displacement (d) is the integral of velocity.

For these calculations, we assumed that m is constant over time. Field observations prior to the Akatani landslide indicate that there may have been earlier deformations on the sliding surface preparatory to the large failure. A precursory gravitational deformation feature was observed on top of the slide area from LiDAR topographic data [*Chigira et al.*, 2012]. This small scarplet suggests that strain due to deformation was accumulating prior to the slide event, in effect preparing a large portion of the sliding surface for failure

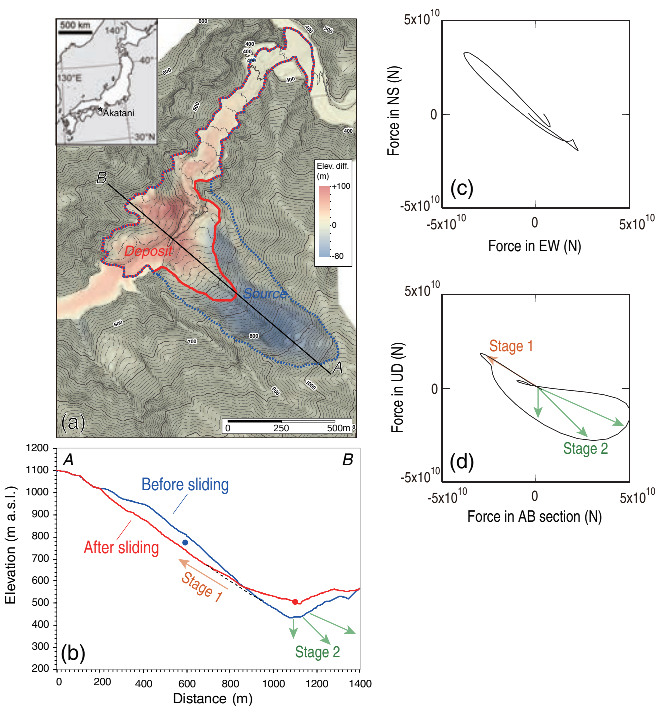

Figure 1. Topography of the Akatani landslide. (a) Elevation changes at the Akatani landslide estimated from airborne LiDAR topographic surveys. Blue and Red contours show the extent of the soil mass before and after the landslide, respectively. (b) Vertical section along the A–B line (see (a) for location) before (blue) and after (red) the slide event. Small circles show the centre of mass before and after the landslide. Arrows correspond to the direction of forces in (d). The vertical axis shows the elevation above sea level. (c) Particle motion of the source time function between 90 and 140 s in a horizontal plane. (d) Particle motion of the source time function between 90 and 140 s in a vertical plane along the A–B line (see (a)).

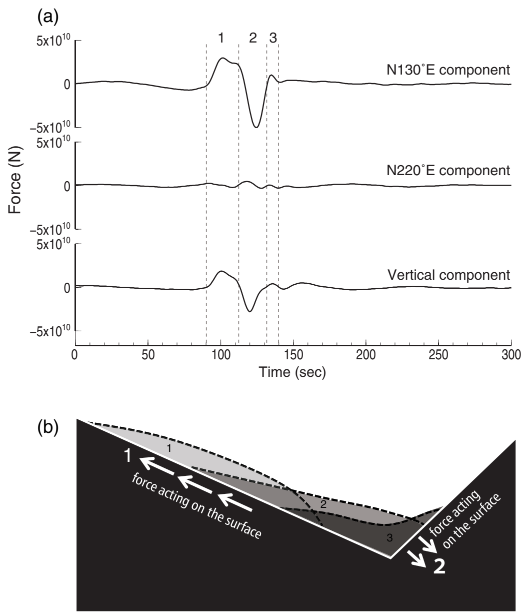

Figure 2. Dynamic process of the Akatani landslide. (a) Estimated single-force source time functions for the two horizontal components (130° and 220° from North) and the vertical component. (b) Schematic diagram of the mass sliding model. The numbers correspond to the three stages indicated in (a).

in 2011. These observations are consistent with our assumption that the entire mass moved relatively uniformly from the beginning. The constant mass assumption is also justified by a typical motion of deep-seated catastrophic landslides, i.e., source-to-deposit translational block movement as observed in a videotaped landslide in 2004 [*Suwa et al.*, 2010] and in a landslide of the 2011 event (Ohto-Shimizu landslide) sighted by residents nearby the Akatani landslide. Additionally, during the first 10 seconds shown in Figure 3e, radiation of high-frequency energy is limited, indicating that destructive failure did not occur at the onset of sliding.

We integrated the estimated three-component source time functions individually, and computed their vector sum to obtain the velocity and displacement (Figure 3b and 3c).

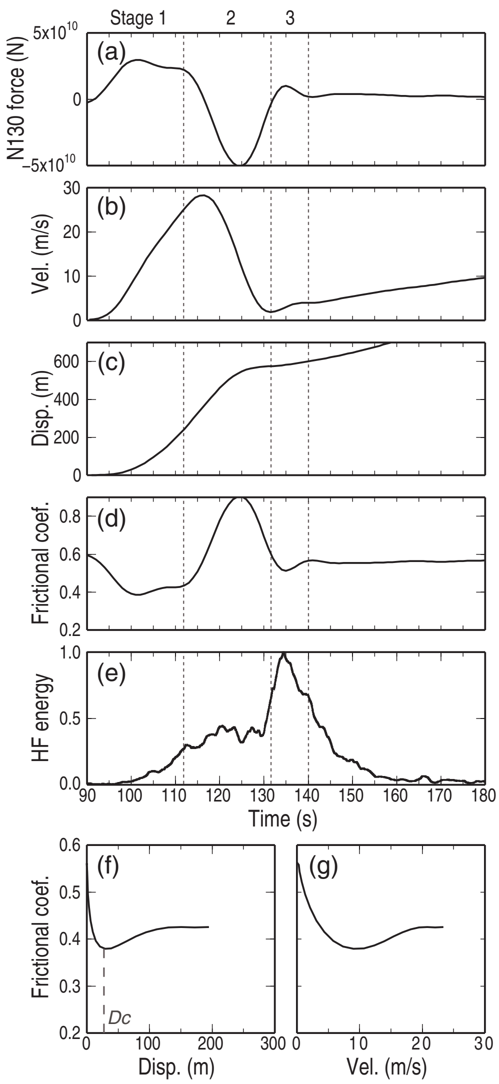

Figure 3. Time histories of dynamic parameters. (a) Source time function in the N130°E component. (b) Estimated absolute velocity of the mass. (c) Estimated absolute displacement of the mass. (d) Time history of the dynamic coefficient of friction obtained from equation (1). The data after the second stage cannot be used for this purpose. (e) Envelope of high-frequency velocity waveforms. (f) Relationship between the dynamic coefficient of friction and velocity in the first stage. (g) Relationship between the dynamic coefficient of friction and displacement in the first stage.

Since long-period noise accumulates when we integrate in the time domain, the increasing trends in the velocity and displacement after the third stage (Figures 3b and 3c) may be due to noise effects. We infer that the motion of the landslide mainly stopped at about 140 sec where the acceleration values are near zero. The maximum velocity was 28 m/s (101 km/h), attained at approximately 116 seconds. The amplitude of the displacement at the end of the second stage was 570 m, which is consistent with the distance the center of the mass travelled during the slide (530 m). The envelope of the high-frequency waveform (1–4 Hz) [*Yamada et al.*, 2012] is also shown in Figure 3e for comparison. This is the average of the 15 normalized vertical velocity waveforms for which station distance was less than 40 km from the landslide location.

The motion of the sliding mass in the direction of landslide propagation can be expressed as:

$$f = mg(\sin\theta - \mu\cos\theta). \quad (1)$$

where f is the inertial force of the sliding mass along the slope, θ is the angle of the slope, and μ is the coefficient of friction. As m and θ are assumed to be constant, the only unknown variable is μ. Therefore, the coefficient of friction during sliding can be obtained directly from equation (1). The estimated dynamic coefficient of friction is shown in Figure 3d. Note that equation (1) only holds in the first stage, as the additional stopping force acts on the mass in the second stage. Therefore, the data from the second stage onwards in Figure 3d cannot be used in this context. During the first 10 seconds, μ drops from 0.56 to 0.38, then remains at approximately 0.4 during sliding. In order to assess the dependency of the coefficient of friction on slip, the relationships between μ and displacement, and μ and velocity are shown in Figures 3f and 3g. The figure shows clear slip-weakening and velocity-weakening, and the steady-state distance (D_c) is estimated to be 25 m.

5. Discussion

The decrease in sliding friction has also been observed during earthquakes [e.g. *Ide and Takeo*, 1997; *Heaton*, 1990] and laboratory rock experiments [e.g. *Hirose and Shimamoto*, 2005; *Han et al.*, 2007]. For large earthquakes, D_c is estimated to be 0.2–1.0 m [*Ide and Takeo*, 1997], an order of magnitude or more lower than our estimate. This difference may be caused by the greater normal stress during earthquakes. For the Akatani landslide, normal stress due to gravitational force is 0.4–0.5 MPa on average, while at depths of about 5 to 20 km where most seismic events occur, the normal stress can be several orders of magnitude larger. Larger normal stress generally equates to a smaller D_c [*Wibberley and Shimamoto*, 2005]. The steady-state coefficient of friction and steady-state distance depend on several factors, including normal stress, slip rate, and material properties of the contact surfaces [*Togo et al.*, 2011]. These conditions are very different from those in laboratory experiments, so it is difficult to use small scale testing to infer dynamic properties of real landslides. Therefore, using this approach to correctly determine parameters of the sliding mass can help in understanding the dynamic friction of actual landslides.

The dynamic coefficient of friction is difficult to measure in the field. Most measurements of the friction coefficient are obtained from the ratio of drop height to runout length [*Scheidegger*, 1973]. *Scheidegger* [1973] proposed an empirical relationship between volume of the landslide and the apparent coefficient of friction based on the field measurements. According to that equation, the apparent coefficient of friction of the Akatani landslide is estimated to be 0.35. A similar coefficient was obtained by *Ashida et al.* [1985]. These values are consistent with our observation of the steady-state coefficient of friction.

The decrease in the coefficient of friction as a function of slip can be interpreted in several ways. One possible explanation is that liquefaction on the sliding surface is induced by excess pore pressure, a process which is widely observed in laboratory experiments [*Sassa*, 1996]. When the Akatani landslide occurred, the hillslope had received in excess of 1000 mm of rainfall over 3 days. As the mass starts sliding, the loosened bedrock is fractured and compacted, causing pore pressure to rise, and triggering liquefaction on the sliding surface. This phenomenon can drastically decrease the frictional force on the sliding surface. Another possibility is that roughness on the sliding surface affect the friction level. Previous studies have discussed how the roughness of sliding surfaces can control the movement of slow landslides [*Mizuno*, 1989]. Deformation of hillslopes [*Chigira et al.*, 2012] may be indicative of topographic features on the slide surface which can contribute to the initial slope support. As the slide initiates and progresses, breaking of these features may cause a drop in the friction and significantly affect the motion of rapid landslides.

We note that the pattern of high-frequency energy radiation is quite different from the low-frequency radiation (Figures 3a and 3e), so the source mechanisms are likely quite different. The high-frequency energy may be related to processes on the sliding surface [*Yamada et al.*, 2012] or internal to the landslide mass. The high-frequency has its peak amplitude during the third stage when the force estimated from the low-frequency waveforms is relatively small. As shown in Figure 1, the sliding mass ascended the opposite valley wall during the second stage. We speculate that this mass fell back and returned in the opposite direction, as suggested by *Evans et al.* [1994]. The internal collision with the returning mass and other complicated processes on the slipping surface may contribute to the high-frequencies during the stopping process.

6. Conclusions

In this paper, we analyzed the seismograms recording the signal produced by the Akatani landslide due to Typhoon Talas, passing Japan Island in September 2011. The high-quality dataset enables us to perform a source inversion and obtain a detailed time history of the landslide process. We showed the changing values of the dynamic friction during the landslide, starting at a relatively high value, and drops to a lower value as the landslide progresses. The change in the frictional level on the sliding surface may be due to liquefaction or breaking of rough patches, and contributes to the extended propagation of the large landslide.

The approach demonstrated here offers an innovative method for understanding the sliding mechanism of landslides and determining parameters, such as slide acceleration and coefficient of friction. In future research, we will accumulate seismic records from slope failures of varying size, and obtain a generalized frictional constitutive law for landslides. Such physical models will help to simulate the motions of mass failure, and contribute to the mitigation of catastrophic landslides hazards.

Acknowledgments. We acknowledge the National Research Institute for Earth Science and Disaster Prevention for the use of F-net data. High-resolution DEM data, which have been used to calculate landslide volumes, were provided by the Nara Prefectural Government and the Kinki Regional Development Bureau of the Ministry of Land, Infrastructure and Transport. We thank Professor Jim Mori in Kyoto University for assisting in the improvement of the manuscript.

References

Ashida, K., S. Egashira, T. Sawada, and N. Nishimoto (1985), Geometric structures of step-pool bed forms in mountain streams, *Disaster Prevention Research Institute Annuals, Kyoto University*, 28, 325–335.

Bouchon, M. (1979), Discrete wave number representation of elastic wave fields in three-space dimensions, *J. Geophys. Res.*, 84, 3609–3614.

Brodsky, E., E. Gordeev, and H. Kanamori (2003), Landslide basal friction as measured by seismic waves, *Geophys. Res. Lett.*, 30, 2236, doi:10.1029/2003GL018485.

Chigira, M., Y. Matsushi, C. Tsou, N. Hiraishi, M. Matsuzawa, and S. Matsuura (2012), Deep-seated catastrophic landslides induced by Typhoon 1112 Talas, *Disaster Prevention Research Institute Annuals, Kyoto University*, 55, 193–211.

Evans, S., O. Hungr, and E. Enegren (1994), The Avalanche Lake rock avalanche, Mackenzie mountains, northwest territories, Canada: description, dating, and dynamics, *Canadian Geotechnical Journal*, 31, 749–768.

Han, R., T. Shimamoto, T. Hirose, J. Ree, and J. Ando (2007), Ultralow friction of carbonate faults caused by thermal decomposition, *Science*, 316, 878–881.

Hasegawa, H. and H. Kanamori (1987), Source mechanism of the magnitude 7.2 Grand Banks earthquake of november 1929: Double couple or submarine landslide? *Bull. Seismol. Soc. Am.*, 77, 1984–2004.

Heaton, T. (1990), Evidence for and implications of self-healing pulses of slip in earthquake rupture, *Phys. Earth. Planet. In.*, 64, 1–20.

Hirose, T. and T. Shimamoto (2005), Growth of molten zone as a mechanism of slip weakening of simulated faults in gabbro during frictional melting, *J. Geophys. Res.*, 110, B05202, doi:10.1029/2004JB003207.

Ide, S. and M. Takeo (1997), Determination of constitutive relations of fault slip based on seismic wave analysis, *J. Geophys. Res.*, 102, 27–27.

Iwaya, T. and K. Kano (2005), Rock densities for the geologic units in the Japanese islands: an estimate from the database PROCK (Physical Properties of Rocks of Japan), *J. Geol. Soc. Japan*, 111, 434–437.

Kanamori, H. and J. Given (1982), Analysis of long-period seismic waves excited by the May 18, 1980, eruption of Mount St. Helens- a terrestrial monopole, *J. Geophys. Res.*, 87, 5422–5432.

Lin, C., H. Kumagai, M. Ando, and T. Shin (2010), Detection of landslides and submarine slumps using broadband seismic networks, *Geophys. Res. Lett.*, 37, L22309, doi:10.1029/2010GL044685.

Mizuno, K. (1989), Landslides of clayey slopes with a wavy slip surface: Model and its implications, *Science Reports of the Institute of Geoscience, University of Tsukuba*, 87–151.

Moretti, L., A. Mangeney, Y. Capdeville, E. Stutzmann, C. Huggel, D. Schneider, and F. Bouchut (2012), Numerical modeling of the mount steller landslide flow history and of the generated long period seismic waves, *Geophys. Res. Lett.*, 39, L16402, doi:10.1029/2012GL052511.

Nakano, M., H. Kumagai, and H. Inoue (2008), Waveform inversion in the frequency domain for the simultaneous determination of earthquake source mechanism and moment function, *Geophys. J. Int.*, 173, 1000–1011.

Sassa, K. (1996), Prediction of earthquake induced landslides, *Proc. 7th Int. Symp. on Landslides, Trondheim, "Landslides"*, 1, 115–132.

Scheidegger, A. (1973), On the prediction of the reach and velocity of catastrophic landslides, *Rock Mech. and Rock Eng.*, 5, 231–236.

Suwa, H., T. Mizuno, and T. Ishii, (2010), Prediction of a landslide and analysis of slide motion with reference to the 2004 Ohto slide in Nara, Japan, *Geomorphology*, 124, 157–163.

Togo, T., T. Shimamoto, S. Ma, and T. Hirose (2011), High-velocity frictional behavior of Longmenshan fault gouge from Hongkou outcrop and its implications for dynamic weakening of fault during the 2008 Wenchuan earthquake, *Earthquake Science*, 24, 267–281.

Ueno, H., S. Hatakeyama, T. Aketagawa, J. Funasaki, and N. Hamada (2002), Improvement of hypocenter determination procedures in the Japan Meteorological Agency, *Quarterly Journal of Seismology*, 65, 123–134.

Wibberley, C. and T. Shimamoto (2005), Earthquake slip weakening and asperities explained by thermal pressurization, *Nature*, 436, 689–692.

Yamada, M., Y. Matsushi, M. Chigira, and J. Mori (2012), Seismic recordings of landslides caused by Typhoon Talas (2011), Japan, *Geophys. Res. Lett.*, 39, L13301, doi:10.1029/2012GL052174.

M. Yamada, Kyoto University, Gokasho, Uji, Kyoto 611-0011, Japan (masumi@eqh.dpri.kyoto-u.ac.jp)